





The nature of crystallographic defects in noncrystalline tubular network block copolymers

Wenpeng Shan^a, Vivek Subramanian^b, Xueyan Feng^c, Edwin L. Thomas^{d,*}

Keywords: Defects, Block copolymer, Self assembly, Tubular network, Gyroid, Diamond, Slice and view SEM tomography

Defects are symmetry breaking features within a crystal. They can be created during growth as well as by applied mechanical forces. We address point, line and surface defects in block copolymer crystals, concentrating on the structure of defects in the tubular network double gyroid and double diamond phases. Experimental results using 3D slice and view scanning electron microscopic tomographic imaging for many types of defects are presented and the nature of the structural details and symmetries are described. Often defects are considered detrimental to the properties and performance of the material, but if the mesoscale defects in 3D periodic block copolymers can be controlled, they can be utilized to achieve various advantageous such as new optical functionalities.

Introduction

There are three general defect classifications in crystalline materials: point, line and surface types, referring to the dimensionality (0, 1 and 2D) of the defect. In atomic crystals, 0D point defects can be, for example, vacant sites (vacancy defect) within the crystalline unit cell, or the presence of an atom in-between normally occupied sites (e.g. an interstitial defect). Such defects do not literally occupy a point but nevertheless are highly localized and their presence only disturbs the crystal symmetry over a very small (a few atoms) region. Line and surface defects, such as dislocations and grain boundaries create a more extensive disruption of the crystal symmetry and correspondingly

Soft matter researchers have long studied various types of defects such as dislocations, disclinations and grain boundaries in liquid crystalline (LC) materials, including the 2D hexagonally packed columnar phase and the 1D periodic smectic A lamellar phase [1–4]. Indeed, the early study of defects in LC phases using optical microscopy was essential for discovery and classification of the structure and symmetries of various possible LC phases via the nature of the symmetry breaking in the optically birefringent phases caused by the defects. The classic text of Kleman (Points, Lines and Walls, [2]) addresses defects in LC matter in great detail and provides important insights into understanding defects, especially relevant to the block copolymer (BCP) cylinder and lamellar phases. Defects in block copolymers have also been

E-mail address: elt@tamu.edu (E.L. Thomas).

Received 6 September 2023; Received in revised form 23 November 2023; Accepted 28 November 2023

^a Biomaterials and Tissue Engineering Research Center, Shanghai Institute of Ceramics, Chinese Academy of Sciences, Shanghai, 200050, China

^b Thermo-Materials & Structural Analysis Division, Thermo Fisher Scientific, Hillsboro, OR, 97124, USA

^c State Key Laboratory of Molecular Engineering of Polymers, Department of Macromolecular Science, Fudan University, Shanghai, 200438, China

 $^{^{\}rm d}$ Department of Materials Science and Engineering, Texas A & M University, United States

produce larger and longer-range stress fields. Interactions amongst neighboring defects lead to various lower-energy arrangements via reduction of the stress fields from defect movement and annihilation.

^{*} Corresponding author.

studied using transmission electron microscopy (TEM), scanning electron microscopy (SEM) and atomic force microscopy (AFM) [5–13]. Recent emphasis addresses defects occurring in $\sim 2D$ thin films due to interest in using BCP for high resolution lithographic masks [14–16]. Early work examined various point defects in monolayers of spherical domains as well as vertically oriented cylindrical domains [14,15]. Defects could be greatly reduced by using so called *directed* self assembly (DSA), whereby 2D chemical and physical templates are utilized to register and control BCP domain patterns [16–19]. Here, the focus is on using vertically oriented lamellae for lithography, where the emphasis is on generating very fine scale, highly controlled, defect-free 2D patterns by eliminating bridging defects, minimizing domain misregistration and domain side wall roughness [16].

In this paper, we study the nature of defects in the double gyroid (DG) and double diamond (DD) 3D continuous tubular network (TN) BCP crystals. Crystalline order in BCPs is not due to symmetrical packing of discrete atoms within a unit cell, but rather arises due to the formation of periodic microdomain structures created by the self assembly of very large numbers of macromolecules. The periodic order arises from the interplay of the minimization of the enthalpic repulsion between the A and B monomers and maximization of the conformational entropy of the respective A and B block chains. For the three canonical BCP microdomain structures, namely spheres, cylinders and lamellae, the shape and symmetry of the rather simple objects that form the periodic arrays are readily identified. However, for the TN structures, the microdomains are both 3D periodic and 3D continuous. By considering the DG and DD unit cells, it is possible to define nonconvex mesoatoms, that occupy specific Wyckoff sites and completely fill the unit cell volume [20,21]. For typical BCP molecular weights, the mesoatoms contain thousands of molecules (each in turn comprised of many thousands of atoms). The unit cell scales with increasing BCP molecular weight and is generally 2-3 orders of magnitude larger in size than for typical atomic crystals. At this much larger 10-100 nanometer scale, the long range crystalline order manifests itself via the shape of the periodic intermaterial dividing surface (IMDS) that separates the microdomains of the BCP [22]. Accordingly, crystallographic defects occur at this larger scale with their influence extending to scales into the micron and above range. For microdomain structures which are continuous, i.e. cylinders, lamellae and tubular networks, the geometry and topology of the defects occurring within the periodic structure can be very different than in atomic crystals due to the one to three dimensional continuity of one or both of the domain structures and as we will emphasize, the adaptability of the mesoatoms to their local environment.

In the simpler lamellar and cylindrical BCP structures, defects can be analyzed from 2D TEM projections. However, to adequately characterize defects in these 3D periodic TN phases requires 3D tomographic structural information. There are several experimental tools that can create tomograms: X-ray ptychometry (XCT) [23], TEM [24], scanning TEM (STEM) [16] and slice and view SEM (SVSEM) [10,25]. Each of these techniques has advantages and limitations. XCT and SVSEM

are the best choices for studying line and surface defects due to the requirement of needing large specimen volume reconstructions to adequately characterize the extended defect structures.

Mesoatoms in tubular network crystals

Quantitative description of defects in TN crystals, requires specification of how the structure is altered from the perfect crystal reference state, which in turn, requires a quantitative description of the reference crystal structure. Of course, the primary distinctive feature of any crystal is the periodic translational symmetry of the contents of the basic unit cell. Combining electron microscopy and small angle X-ray scattering investigations of BCPs [e.g. [26,27]], we know the DG and DD structures each consist of two interpenetrating (inter-catenated) labyrinthine microdomains residing on opposite sides of a triply periodic minimal surface (TPMS). Fig. 1a and b shows the tubular networks surrounded by the colored IMDS within their respective unit cells. However, such a depiction does not yet identify the mesoatoms within the unit cell, nor does it allow for ready assessment of an important characteristic, namely their 3D topology, which distinguishes these tubular networks from all the other BCP phases. To appreciate the topology of the domain networks, a thinning algorithm can be applied to each of the tubular microdomains to define a skeletal graph or network graph, comprised of a set of nodes connected by line segments. Thus, the pair of achiral DD networks are 4-connected (Fig. 1c), while the DG has an enantiomorphic pair of 3-connected networks (see Fig. 1d). The basic 3 and 4 node networks have been previously described by Wells in his book, "Three Dimensional Nets and Polyhedra," as the 10,3-a and 6,4 periodic nets [28]. Wells mentioned that he knew of no material that exhibited a structure based on the racemic mixture of D and L 10,3-a nets, but pointed out that Cu₂O was an example of two interpenetrating 6,4 nets. Wells' network notation is in reference to the smallest fundamental loop in the network. For the DG, this loop consists of 10 nodes, each node having 3 equal length connecting segments meeting at 120° (node functionality, f = 3). To describe loops more generally, we employ the notation $X - Y^n$ where X is the number of nodes, Y is the node functionality and n is the number of consecutive nodes in the loop. Hence for DG, the fundamental loop is $10 - 3^{10}$.

The two enantiomorphic 10,3 graphs in the bcc DG unit cell contain a total of 16 nodal positions which are located on Wyckoff site 16b with dihedral D_3 point group symmetry (3 fold axis with perpendicular 2 fold axes) in space group #230, Ia3d. The two interpenetrating achiral 6,4 graphs of the DD are in a primitive cubic DD unit cell with 2 nodal positions corresponding to Wyckoff site 2a with tetrahedral T_d point group symmetry (4 fold roto-inversion axis, 3 fold axis with 2 fold axis and mirrors) in space group #224, Pn3m. The smallest fundamental loop in DD has 6 nodes, each node having 4 equal length struts meeting at 109.5° (f=4, with the fundamental loop denoted as $6-4^{\circ}$). In addition to the pair of minority component microdomains, the majority component microdomain which surrounds the tubular networks is also 3D continuous and can be described as a slab-like domain that is in the case of the DG, bisected by Schoen's triply

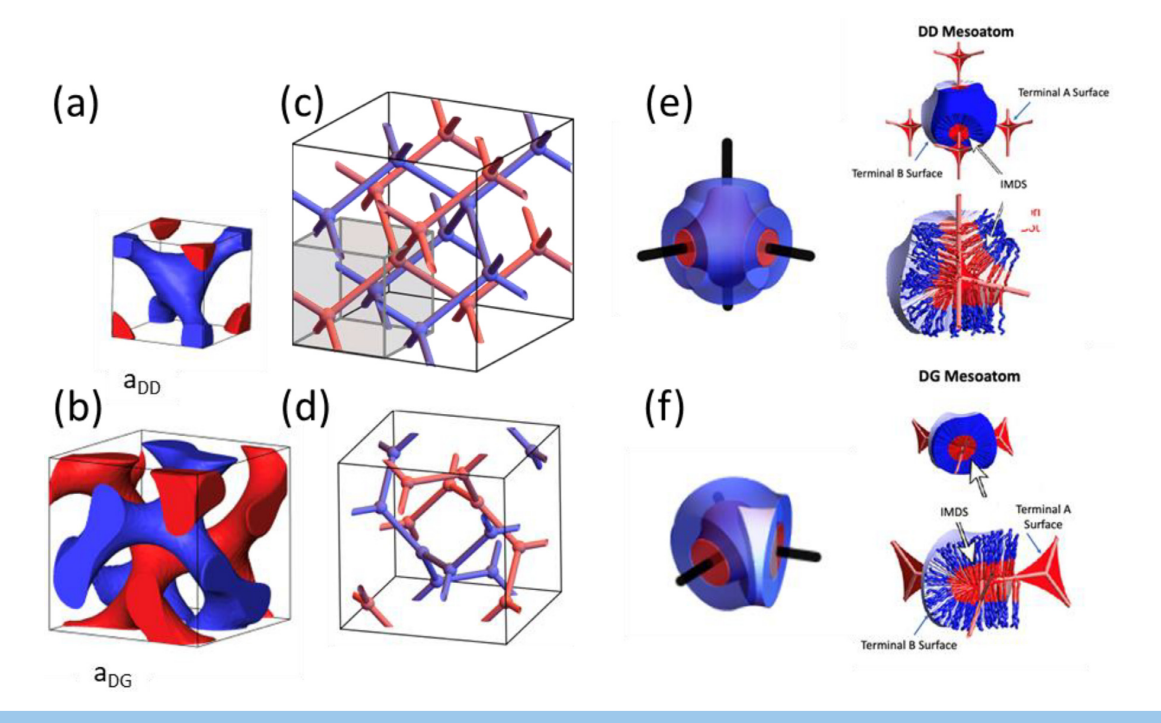


Fig. 1

Block copolymer tubular network crystals, their unit cells, skeletal graphs and mesoatoms, intermaterial dividing surfaces and terminal surfaces. (a, c, e) DD (b, d, f) DG. Some images by permission from [42]

periodic minimal surface (TPMS), called the gyroid (or G surface) and for the DD, bisected by Schwarz's TPMS called the diamond (or D surface).

The next issue for our perfect crystal reference state is to define appropriate finite structural units (the mesoatoms) with the required point group symmetries that can occupy the Wyckoff sites and can link together to create the 3D continuous DG and DD microdomain structures that fill all space. (Details on mesoatom construction are given in [21,29]). Each mesoatom is divided into its minority and majoring block components by the IMDS with the minority block surrounding the skeletal graph and the majority block spanning outwards from the IMDS to the TPMS. Characterization of mesoatoms also includes defining inner and outer terminal surfaces (TS) where the end of the respective polymer domain brushes tend to be located. The outer TS is close to the TPMS while the inner terminal surface appears as a web spanning the skeletal graph (see [21]). Fig. 1e and f show the nonconvex DD and DG mesoatoms, the IMDS, the skeletal graphs and the inner and outer TS. Since a BCP is a one component system, the composition (volume fraction) is the same in any volume containing all the blocks attached to the portion of the IMDS within that volume.

In addition to the ideal crystal mesoatoms, we can also identify various mesoatoms within the core region of defects, so called 'defect mesoatoms'. Generally, near the defect core the translational symmetry is broken, and specification of the shape, size, numbers and types of such 'defect mesoatoms' depends on the details of the particular defect.

Distortions in BCP crystals

Often the unit cell structure of BCP TN crystals departs significantly from cubic, even in the absence of crystallographic defects due to strong nonaffine distortions induced during self assembly processing (e.g. highly anisotropic shrinkage during solvent evaporation) [30,31]. Soft matter unit cells also readily deform under applied mechanical forces [32]. Processing conditions and applied loads generally create nonaffine displacements leading to variations in strut lengths and interstrut angles, resulting in noncubic (triclinic) unit cells with the corresponding loss of precise crystallographic point and space group symmetries. Due to the malleability of the mesoatom networks, such distortions change the local geometry but generally take place without network topology changes since no struts are broken and no new bridging struts are created. We will note these distortions but our main aim is to address crystallographic defects.

Crystallographic defect descriptors in BCP crystals built from mesoatoms

Departures from perfect crystal symmetry in materials range from thermal fluctuations, to kinetically trapped non-equilibrium structures (e.g. the aforementioned processing-induced distortions), to crystallographic defects – it is the latter which are our focus. The most common point defects in atomic crystals are vacancies and interstitials. These are quite straightforward to describe: a vacancy defect occurs when a normally occupied Wyckoff site in an atomic crystal is vacant. An interstitial defect is

an atom located on a site within the unit cell that is not normally occupied. Line defects in crystals are dislocations and are described by the dislocation line vector t (a unit vector locally tangent to the (generally 3D curved) dislocation line and the dislocation Burgers vector \mathbf{b} , a vector giving the magnitude and direction of the displacement generally corresponding to the magnitude of the smallest translational period of the structure. Dislocation motion results in plastic deformation due to the motion of the line defect over its slip plane (the plane(s) containing both tand **b**). There are two limiting dislocation types: edge and screw. Pure edge dislocations have their Burgers vector everywhere perpendicular to the dislocation line vector, while the Burgers vector is everywhere parallel to **t** for pure screw defects. A general dislocation (called mixed) will exhibit variable amounts of edge and screw character along its curved line vector. Dislocation lines must form loops or join into a dislocation network or to a grain boundary or external surface. The most common type of surface defect is a grain boundary. This defect occurs in the region between two impinging crystals having different orientation. The structural description of a general grain boundary in a 3D periodic crystalline material requires 5 variables: 3 variables to specify the relative orientation of the two grains, and two variables to specify the normal to their common boundary plane [3]. As we shall see, the network topology, the fact that the entire structure must be uniformly filled with BCP molecules and the ability of the material to form new types of defect mesoatoms, dictates that the structural descriptors of the many types of defects in TN phases are quite complex.

A simple way to anticipate the nature of some types of defects in periodic TN crystals is to reference the many known types of defects in diamond networks (space group #227, Fd3m), where the sp³ bonding results in single diamond network crystals. Because carbon, silicon and germanium are important materials and defects strongly influence their electronic as well as mechanical properties, a huge amount of defect characterization and modeling research has been done on these materials. With continued advances in high resolution 3D imaging, many examples of atomic level resolution of defects, including many types of dislocations and grain boundaries have been revealed [33,34]. Moreover, interactions between various defects will occur such that each defect type can modify the other, resulting in new atomic configurations for various defect–defect reactions [35].

In general, symmetry breaking defects in TN crystals involve topological changes to the network(s) along with strong alterations to the mesoatoms situated near the core region of the defect. Mesoatoms are therefore highly malleable-adaptable and can readily alter their volume and shape by (partial) merging/separation via exchange of molecules with their connected neighbors, leading to variable node–node separation distances as well entirely new mesoatom symmetries. These mesoatom adaptations create variable strut (bond) lengths, interstrut (bond) angles, and importantly, new node functionalities. There is essentially a continuum of degrees of freedom in terms of the deformation possibilities of mesoatoms, which results in a very wide spectrum of possible defect morphologies. This morphing ability is a direct consequence of the mesoatoms being comprised of huge numbers of highly flexible polymer molecules allowing

cooperative rearrangements as facilitated by the motion of the A-B covalent junctions over the 3D continuous IMDS. These facile molecular movements generally do not require an A block to unfavorably transit through a B block domain (or vice versa).

The distances between the IMDS and inner and outer TS interfaces in and around any defect cannot deviate much from the preferred spacing of the respective block trajectories. The optimum distances are a tradeoff between the desire of the BCP molecules to assume high entropy conformations and the need to minimize interfacial area while uniformly filling space. The core region of defects is an attractive location for impurities. For BCPs, these would likely arise from nonidealities in the synthesis: homopolymers as well as blocks with different compositions and molecular weights. 3D reconstructions of specific defects should be able to help characterize the amounts and type of impurities present in the defect core region, especially by purposeful blending of a known molecular weight and amount of the additive. The presence of defects alters not only the minority A domain shape and, ofttimes, the node connectivity but also modifies the outer majority B mesoatom shape since the B regions on neighboring mesoatoms must provide compatible, complementary terminal surface shapes in order to fit smoothly together to create a 3D continuous B matrix that uniformly fills and separates the A networks [20,21]. Overall, defect mesoatoms exhibit sizes and shapes that are dictated by their surroundings, an often highly variable environment.

Point defects in TN phases

Two of the simplest point defect types are the minority network break defect and minority network - network bridge fusion defect. Respectively, these defects decrease or increase network domain continuity and thus alter the network topology. Fig. 2a shows a pair of DD network break defects which might have formed due to local excess extension of the network struts that then lead to local strut thinning with increase in the IMDS area and unfavorable majority and minority block conformations. Such strain-induced distortions could be subsequently relieved by introducing network breaks with modification of the IMDS and repositioning of the block junctions and A and B chains, resulting in the observed tapered, smooth cone-shaped struts (Fig. 2a). Inspection of the surrounding neighborhood of these break defects shows that the structure rapidly relaxes into the long range ordered crystalline state. Bridge defects occur whenever the node functionality increases above f = 3 for DG or above f = 4 for DD. Such defects might occur during growth when a mesoatom located in a position near two growing networks, reconfigures to its surroundings and links the networks, resulting in a new type of mesoatom with increased node functionality and mesoatom volume. For example, the DG bridge f = 4 defect in Fig. 2b connects the red (RH) network to the blue (LH) network via the green bridges [10].

Interestingly, a bridge defect results in new types of loop defects due to the alternation of the number and nature of the set of mesoatoms in a closed network loop from the normal fundamental network loop. For example, as is evident from Fig. 2b, the networks are altered from the normal $10-3^{10}$ DG loops as the f=4 bridge defect creates a 9 node red loop (9-

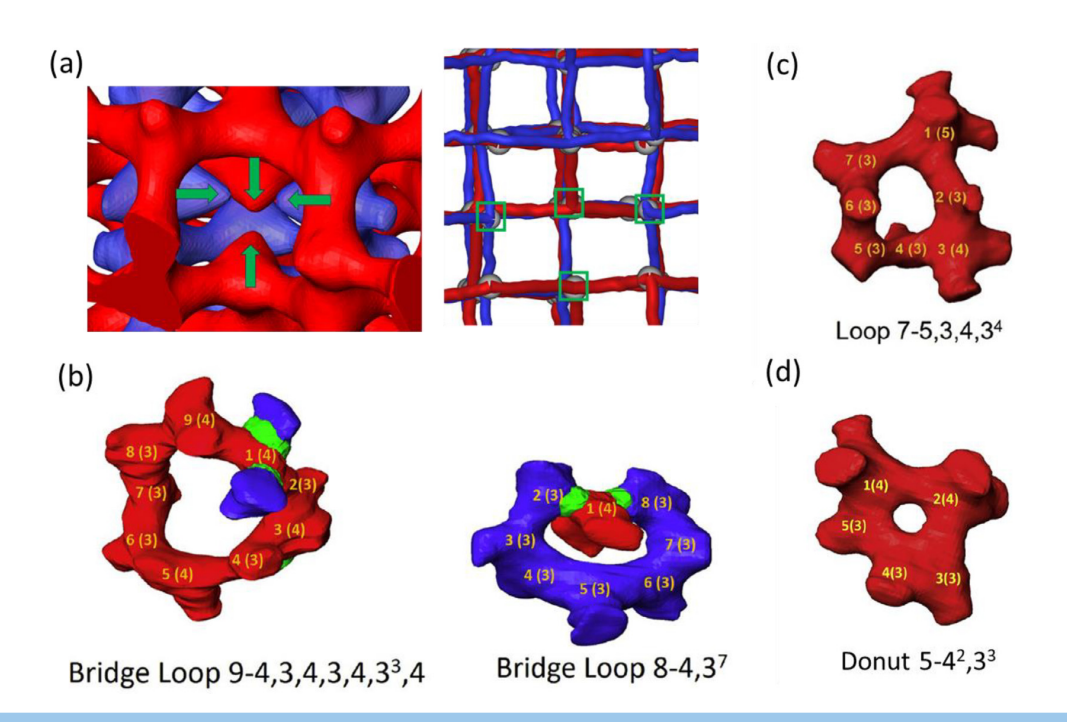


Fig. 2

Point defects in tubular networks (a) SVSEM reconstruction of a pair of DD strut break point defects, one in the blue network and one in the red network (see green arrows). The strain field of these break defects is quite local as evident from the approximate retention of the 4 fold roto-inversion symmetry of the skeletal graph as viewed along the [001] direction. (b, c) DG point defects. Bridging point defect joining two loops in DG. (d) Donut defect in DG. Images in (b–d) by permission from [10].

4,3,4,3,4,3³,4) and an 8 node blue loop (8-4,3³), where the first number indicates the number of nodes in the loop and the subsequent numbers indicate the sequence of node functionalities around the loop. The f=4 node is included in both loops. The remainder of the blue loop is comprised of normal DG LH f=3 mesoatoms, whereas the red loop contains 3 additional f=4 mesoatoms which in turn strongly alters the surrounding network topology and node chirality.

Node functionality f = 5 defects are also found in DG networks [10]. These higher functionality nodes have even larger volumes and create many more bridges between more loops. Such a large f = 5 mesoatom tends to shrink the size of adjacent mesoatoms and their loops. For example, Fig. 2c shows a f = 5 node in a 7-5,3,4,3⁴ loop, demonstrating that node functionality and loop size are interdependent.

The presence of point defects also affects network intercatenation since a loop with a smaller number of nodes leads to a smaller central opening which if too small, cannot be threaded by the second network. This in turn forces alteration of the normal structure in the adjacent regions leading to additional defects. Fig. 2d shows a small, non-catenated 5-4²,3³ loop. Such non-catenated loops have been termed "donuts". This coupling of node functionality defects and network topology necessitates the occurrence of additional defects and extends the symmetry breaking outwards over a larger region. Thus, while break point defects create only a rather local structural perturbation, on the other hand, bridge defects extend their influence over a significant

volume of material and necessitate creation of multiple types of additional defects. Overall, point defect descriptors in TN structures must therefore be more extensive to fully describe the more numerous degrees of freedom available to altering the mesoatoms and their loops from those in the equilibrium defect-free reference crystal.

Line defects in TN phases

To identify and understand the structure of a dislocation defect, one needs to be able to view a much larger 3D region than for point defects. Characterizing the dislocation requires distinguishing both the line vector and the Burgers vector. Once the defect core region is identified, then a Burgers circuit that starts on a normal lattice point or on a mesoatom node (Wyckoff site) and passes completely around the defect line using steps with translational symmetry from point to equivalent point or node to equivalent node is constructed (for double networks, there would be two Burgers circuits, one for each network). For a circuit constructed in a region in a perfect crystal, the closure failure of the circuit will be zero, while the circuit enclosing the defect line will have a closure failure corresponding to the Burgers vector of the defect. Since the dislocation line energy scales as the square of the Burgers vector, the most favorable line defects will be those with the smallest Burgers vector. If the defect is a socalled perfect dislocation, the motion of the dislocation displaces the structure by some (normally smallest possible) lattice vector, so as such defects move over their slip plane, the crystal is simply

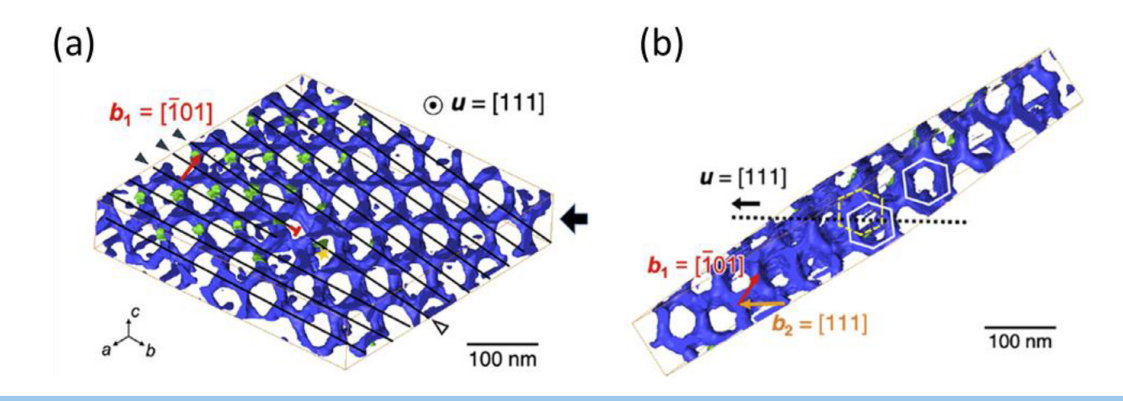


Fig. 3

Dislocation line defect in DG. (a) View along the dislocation line for the left handed gyroid network. (b) View transverse to the dislocation line showing the mixed Burgers vector components b_1 and b_2 . The small green regions in 4a are locations where there are bridge defects between the two DG networks. Reprinted with permission from [11].

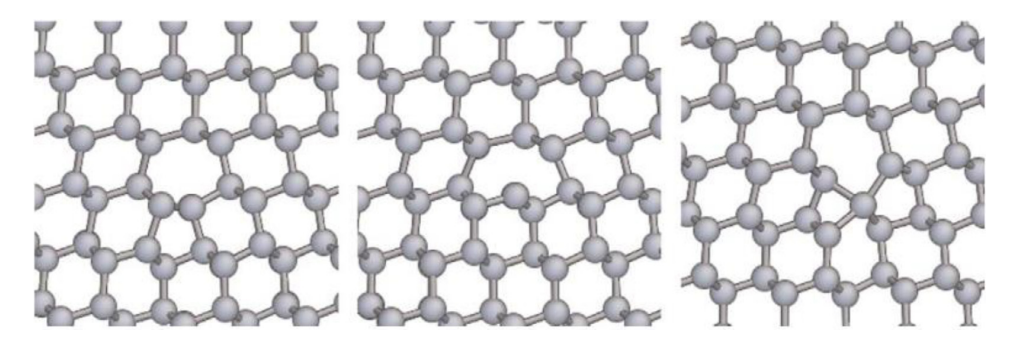


Fig. 4

Computed atomistic dislocation core structures in a single diamond network viewed along the dislocation line. (111) Planes are horizontal. Figure used with permission from [33].

shifted across the slip plane and maintains its regular periodic state. However, in some situations, the strain energy of the defect can be lowered by dissociation of the perfect dislocation into a pair of partial (imperfect) dislocations connected by a few unit cells wide stacking fault [34]. Since the DG has a bcc unit cell, the lowest energy dislocation defect would have the shortest translation vector: $\mathbf{b} = a_{DG} (<111>)/2$, while for the DD, with a primitive cubic cell, the lowest energy dislocation would have $\mathbf{b} = a_{DD} < 100>$.

Only a single paper has thus far addressed dislocation defects in BCP TNs [11]. Because the investigation employed TEM analysis of a thin microtomed section of a DG BCP, just a short length of dislocation could be analyzed (see Fig. 3a). The dislocation line was along the [111] direction with mixed character, $\boldsymbol{b} = a_{DG} < 0.012$, which would indicate a more than 600 % increase in the dislocation line energy compared to the expected $\boldsymbol{b} = a_{DG} < (-1.011) < 0.000$. Surprisingly, the neighborhood surrounding the defect also contained a region exhibiting a 2D periodic array of f = 4 network bridge defects (indicated by the green regions in Fig. 3a).

Some insight on other types of line defects that will likely be encountered in DD crystals can be gained from inspection of defect core configurations in atomic diamond network materials determined by high resolution TEM and atomic modeling [33]. Fig. 4 taken from [33] shows views along the dislocation core (the [110] direction normal to the plane of the figure) for three different dislocation types in silicon. As is evident, the basic 6-4 diamond loops are altered in the core region to a pair of 7 node and 5 node loops or a single 8 node loop or a triplet pairing of a 7, a 5 and a 4 node loops. The structure reverts to the normal diamond network within a few unit cells of the dislocation core. In addition, some work on dislocation structures in Cu_2O which has the double diamond network structure has been done.

Surface defects in TN phases

As with dislocation structures, the structural details of the enormous variety of types of grain boundaries in tubular networks have only begun to be investigated. Indeed, sometimes to understand a complex family of structures, working to identify and analyze a few specialized, simple structures affords recognition of key aspects of the structures and a good pathway forward. One of the simplest grain boundary types is a twin. In a twin boundary (TB), the boundary plane is a mirror plane between the adjacent grains. Such TBs are quite numerous in all crystalline materials since they have a relatively low energy defect core structure. Twins can be either formed during growth or by

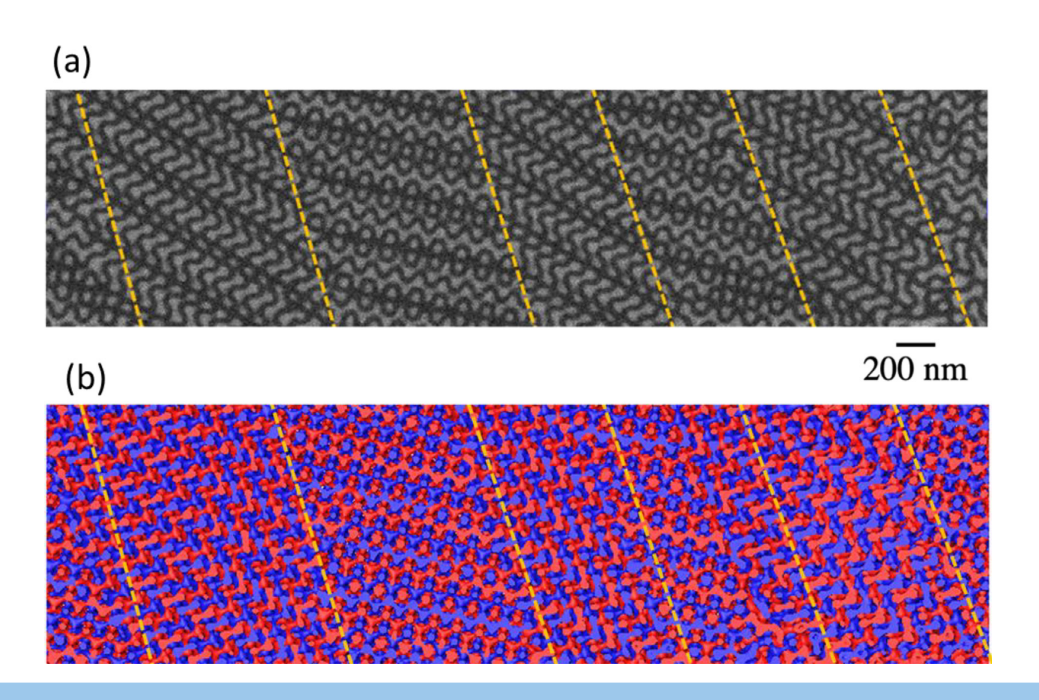


Fig. 5

Twin boundaries (a) SEM slice image of 6 parallel twin boundaries in a PS-PDMS sample. The bright regions are the PDMS minority network domains and the PS matrix is dark. (b) 3D SVSEM reconstruction. This volume containing about 5400 unit cells is readily segmented into three 3D continuous networks: two PMDS and one PS, indicating the absence of any network bridge type defects.

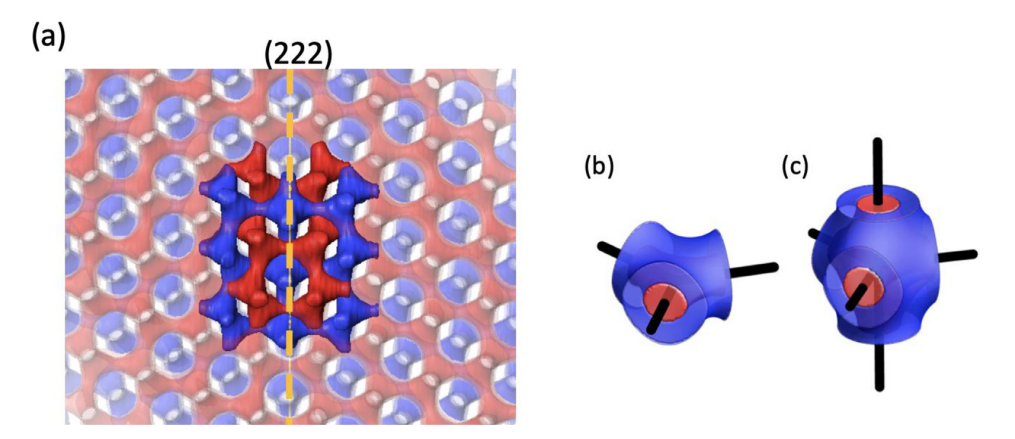


Fig. 6

A twin boundary defect (mirror plane indicated by the vertical dashed orange line) visualized by 3D SVSEM tomography creates two new types of DD mesoatoms. (a) The (222) twin boundary in the DD phase as viewed along [112]. (b, c) Two new types of mesoatoms having f = 3 and f = 5 are formed on the TB, both with D_{3h} point group symmetry instead of the T_d tetrahedral symmetry of normal DD mesoatoms. Permission from [12].

mechanical deformation. Twin boundaries often appear as parallel boundaries in elongated grains, as for example, in the SVSEM image in Fig. 5 which shows a set of 6 parallel twin boundaries in a PS-PDMS DD TN sample.

For the DD TB, one could anticipate based on the cubic diamond-tetrahedral symmetry, that the structure might mimic aspects of the (111) TB in (single) diamond crystals like silicon. Indeed, viewing the DD TB along the parallel and normal directions, one of the two diamond networks (colored red in Fig. 6) in a DD BCP crystal containing a TB has precisely the same

network structure as the single network twin in silicon [12]. The mirror plane coincides with the (111) plane and bisects the BCP struts (corresponding to the Si bonds) with all nodes/mesoatoms retaining their T_d point group symmetry. In the BCP defect, the nodes of the second BCP diamond network (blue color) lie *on* the TB (222) plane. The malleable T_d mesoatoms morph their symmetry and link up into planar hexagonal 6-(5,3)³ loops. Because a twin boundary is a highly symmetrical defect, it is straightforward to identify two new types of defect mesoatoms, a f = 5 and a f = 3, each having D_{3h} symmetry.

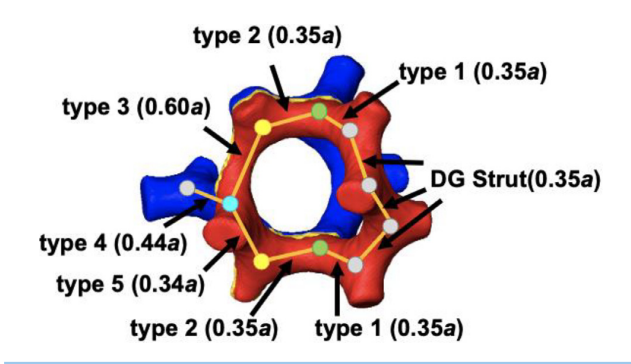


Fig. 7

New DG mesoatoms types with a new DG loop due to a TB. Level set model showing the 5 types of struts on the (422) TB. The strut lengths are given as fractions of the unit cell parameter a of the DG. The mirror boundary plane (gold interface between red and blue networks) separates a right (red) network from a left (blue) network. 5 types of boundary struts are identified. Grey colored nodes for the normal f=3 DG nodes, green indicates new f=3' boundary nodes, yellow indicates another type of new f=3'' boundary nodes, and aqua indicates a new f=4' boundary node. The skeletal graph of the TB loop is $9-4',3',3'',3^4,3'',3''$.

Remarkably, the DG phase with Ia3d cubic symmetry does not contain any mirror symmetry elements, but twins do indeed appear in the DG and are located on (422) planes [36]. Such defects act as topological mirrors since the two interpenetrating networks in the DG are enantiomorphic, so the respective network chiralities switch as the networks cross the TB. Three new types of defect mesoatoms are formed as these reside on the boundary and must have mirror symmetry, unlike the D₃ point group of the normal DG mesoatoms. The TB creates a new type of loop comprised of 9 nodes: 9-4',3',3",3⁴,3",3' (see Fig. 7). This new type of loop contains 4 normal DG mesoatoms that are positioned off the boundary and coherently join to the normal DG 10-3¹⁰ network. There are 5 mesoatoms located on the mirror boundary and these must adjust to become mirror-symmetric: one is a new type of f = 4' and two are new types of f = 3' and 3" mesoatoms (where the prime symbol denotes a mesoatom with different shape and strut lengths and inter-strut angles than the normal DD f = 4and DG f = 3 mesoatoms). Thus, malleable mesoatoms are key to forming twin boundaries in both DD and DG. Twins feature a smooth, continuous IMDS without any network bridge or break point defects as well as allowing networking inter-catenation.

General grain boundaries involve both tilt and twist of the relative orientation of the unit cells in the adjoining grains. In hard matter systems, the coincident site lattice (CSL) concept is used to search for special low energy boundaries where for certain geometrical relations, there is commensuration of a 2D array of normal lattice sites in both grains. One anticipates that for TN BCPs, low energy coincidence boundaries will also likely appear for certain special values of tilt and twist that result in coherent matching of a 2D array of the outer faces of mesoatoms across the grain boundary likely accompanied by some relaxation of the mesoatoms between these sites. Possible candidate boundary planes for such coincident site boundaries can be estimated from comparison of superposed low index slices using level set models.

An interesting aspect of grain boundary surface defects is that when three grains meet, they create a type of line defect termed a triple junction line (TJL) defect (see Fig. 8a). Yet another type of point defect occurs when a set of 4 triple junction lines merge to form a quadruple point (Fig. 8b). An SEM image of a region with a triple junction in a DD sample is shown in Fig. 8c. Thus, 2D defects (grain boundaries) can interact to create a network of 1D defects (TJL) having a set of 0D defects at their vertices. The grain structure itself creates a type of 3D network structure, somewhat akin to a 3D collection of soap bubbles, consisting of grain boundaries, triple junction lines and quadruple points. The mechanical and thermodynamic stability of TJL networks have been studied for metallic systems and the geometry of some TJLs has been modeled by using the coincidence site lattice approach [37]. The structural details of the grain boundaries in TN BCPs and especially that of the triple line are under study using SVSEM.

Another type of defect often encountered in hard matter is a thin noncrystalline region located between crystalline grains. Such regions can be due to incomplete crystallization between adjacent grains or can occur due to segregation of noncrystallizable impurities to the GBs. Fig. 9a shows a thin disordered, microphase separated region between DG grains. The disordered region is not a homogeneous mix of the two blocks but is microphase separated into a type of continuous random network (CRN). The 3D reconstruction shows that the disordered region is a single continuous 3D network comprised of linked variations of the basic f = 3 DG mesoatom. Importantly, SVSEM enables measurement of a very large specimen volume allowing statistical distributions of structural features, e.g. histograms of strut lengths. Details of the interface region between the ordered grain and the disordered region are shown in Fig. 9b. The viewing direction of the ordered DG grain is [111] as evident from the 3 fold rotational symmetry in the skeletal graph. The skeletal graph of the disordered region reveals that about 90 % of the nodes (845 independent measurements) have f = 3, with a range of strut lengths, strut directions, and dihedral angles, mesoatom volumes, IMDS curvatures and surface areas as a consequence of the lack of crystalline order. Moreover, there is only one network constituting the disordered phase and there are no unconnected portions of the network. The single CRN resembles the atomic structure of amorphous arsenic with f = 3. A similar type of disordered phase occurs in surfactant-water systems and is termed the sponge phase [38]. Future work following how the sponge phase transforms into the DG phase (and similarly, how a sponge phase with f = 4transforms into the DD phase) may reveal the mechanism(s) of how primordial mesoatoms might reorganize into crystalline tubular networks [21]. In this instance, particular local mesoatom arrangements may serve as nuclei for growth of the crystal with the introduction of small crystalline regions acting as symmetry establishing "perfect defects" in the amorphous CRN which requires splitting the single sponge network into the two intercatenated ordered networks.

Defect-defect interactions

As with other crystalline materials, the various types of defects present in a BCP TN sample will interact when there are adequate driving forces. For example, an interesting variation in the

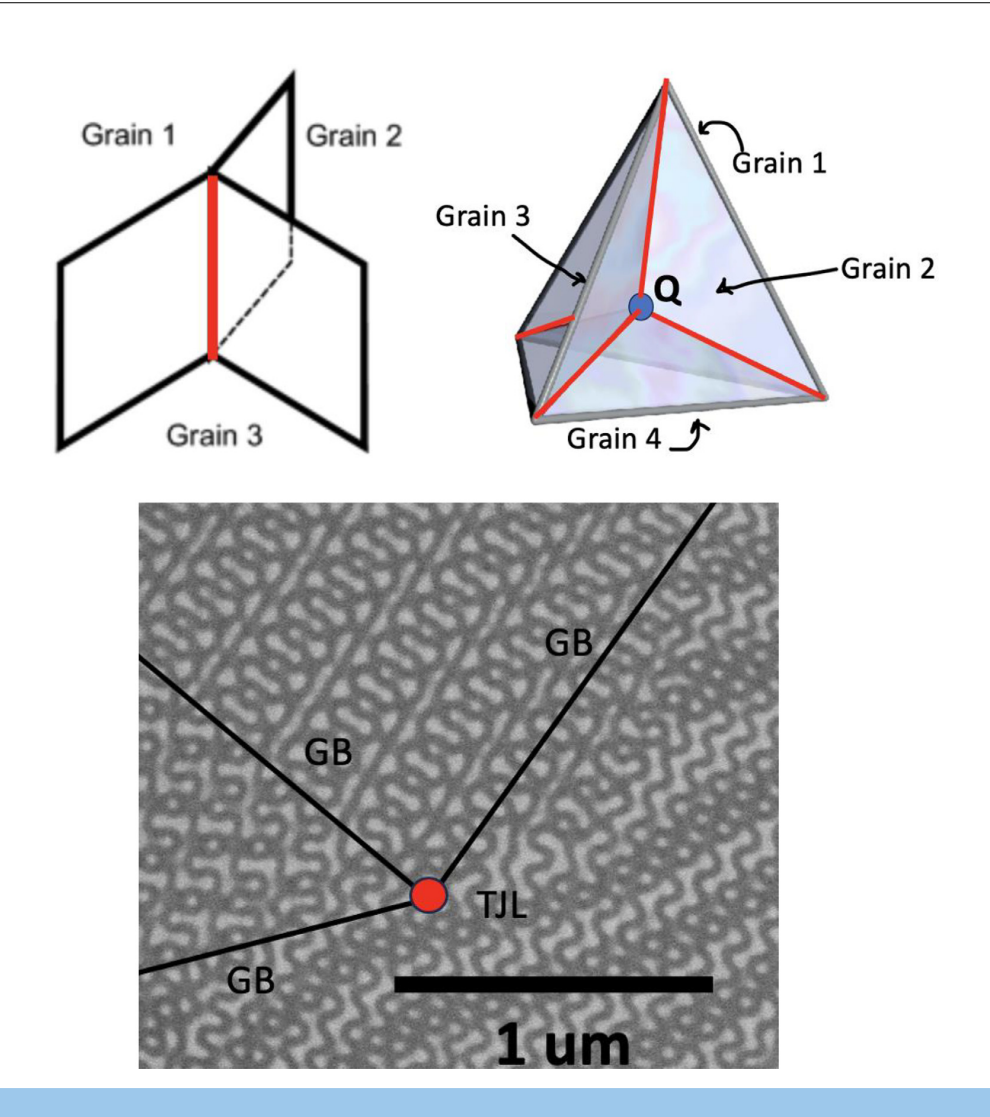


Fig. 8

(a) Schematic of triple junction line (red) formed at the intersection of 3 grains. (b) Quadruple point (Q) at the convergence of 4 triple lines (c) End-on view of a TJL formed at the intersection of 3 DD grains in a PS-PDMS diblock.

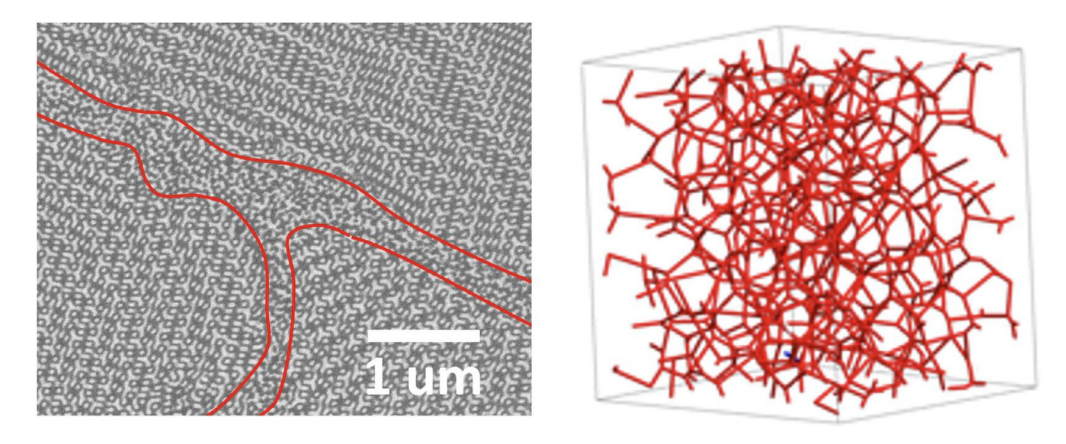


Fig. 9

(a) Noncrystalline continuous random network sponge-like phase located at the boundaries of three DG grains. (b) Skeletal graph of a portion of the DG sponge phase showing that most nodes are f = 3.

Dislocated (222) Twin Boundary

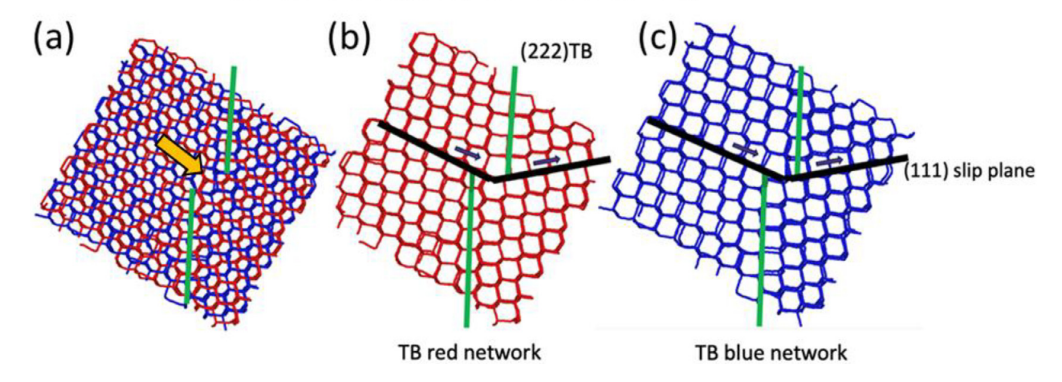


Fig. 10

Defect-defect interactions. (a) Pair of skeletal graphs from a SVSEM 3D reconstruction of a region containing a (222) TB (green vertical line) in a DD grain. (b, c) Red/blue skeletal networks showing the TB and the (111) slip planes (black lines) and the displacement direction (purple arrows) of the boundary due to the passage of a dislocation.

structure of a TB is shown in Fig. 10. Instead of a planar structure, the edge-on view of this DD (222) twin boundary as visualized by the skeletal graphs, shows a kink-like step (orange arrow in figure 10a). One possible explanation for this compound defect is that the TB was deformed by the passage of a dislocation that displaced the TB over a particular slip plane by an amount equal to the Burgers vector. The dislocation is not in the field of view, but we can see the effect of the passage of the dislocation over the slip plane and across the TB. The black line denotes the (111) slip plane that undergoes reorientation on crossing the TB. The purple arrow indicates the direction and amount of the displacement. Since the slip plane changed direction due to the presence of the TB, the dislocation also changed direction (cross slip) and laterally displaced the green TB. The data suggests the slip plane is a (111) plane with the Burgers vector equal to $a_{\rm DD}$ [1 $\bar{1}$ 0].

Summary

With continued advances in tomographic techniques and sample processing strategies, significant new information and insights will be forthcoming, enabling quantitative description and fundamental understanding of a plethora of defects and defect structures in tubular cubic network phases. Up to the present, the crystallographic defects discovered in the DD and DG tubular network phases have striking correspondence with similar defects in tetrahedral diamond and trihedral arsenic network atomic crystals, but the length scales of the various defects differ by factors of 100X to 1,000X. Clearly symmetry and energy minimization, while having completely different atomic vs. molecular details, share much common ground due to the nature of the point and space group symmetries involved and the need to minimize the defect energy. It is apparent that the known influences of defects on bond lengths, bond angles and topology of atomic networks are like the influence of defects on strut lengths, strut angles and topology of BCP networks comprised of mesoatoms. However, unlike the single diamond and single gyroid networks in hard atomic materials, the double networks in soft matter, are comprised of malleable and highly adaptable mesoatoms containing thousands of flexible molecules providing even richer geometric and topological environments for defects and their associated "defect mesoatoms". More complex defect descriptors will also need to be developed to appropriately characterize the defect structures in 3D tubular soft matter. To date, research has found break and bridge point defects, defective loops and donuts, twin boundaries, dislocations, kinked twins, grain boundaries, triple junctions, and disordered noncrystalline sponge phases. These are just the beginning of a what should become the soft matter equivalent of the pursuit of "defect engineering" where purposeful introduction, manipulation and interaction of defects can provide access to otherwise impossible properties with exotic behavior. For example, breaking inversion symmetry in the double gyroid results in a material with a band structure containing Weyl points which should enable angular filtering of light as well as very high power, single mode lasers [39-41]. It should be noted that in this instance of creating a special optical behavior, the parity breaking (loss of inversion symmetry) defects were fabricated in silicon for the microwave regime (centimeter length scale) to be precisely located within every unit cell. BCP molecules are big, slow and many can be heated to induce transformations and then conveniently cooled and arrested below their glass transition temperature for detailed examination at room temperature. Temporal variation of defect responses to applied stimuli [43] and the role of defects in order-order phase transformations is just beginning.

Methods

Slice and view SEM data

SVSEM data were obtained using the procedure reported in [10] and a Thermo Fisher Helios NanoLab 660 Scanning Electron Microscope-Focused Ion Beam (SEM-FIB) DualBeam system. A 30 keV gallium ion beam at a beam current of 80 pA was used to mill the polystyrene (PS)-b-polydimethyl siloxane (PDMS) diblock sample. Secondary electron (SE) imaging was done using a one keV electron beam and beam current of 50 pA. The stronger scattering from the higher atomic number of Si atoms in the PDMS results

in stronger SE emission and provides excellent intrinsic contrast between the PS and PDMS domains. Fiducials were used to register the FIB and SE images during the automatic slice and view process. The resolution for the 2D SEM images is approximately 3 nm/pixel and the FIB slice thicknesses is about 3 nm/slice. Based on the binarized images, a 3D volume can be reconstructed as colored (red/blue) PDMS networks within a transparent PS matrix using Avizo software.

Materials and sample processing

The polystyrene-b-polydimethylsiloxane (PS-PDMS) diblock copolymers were synthesized by sequential polymerization of styrene and hexamethylcyclotrisiloxane [44]. A 50 kg/mol PS and 33 kg/mol PDMS having a PDMS volume fraction of 41 % was solvent cast into a thin film over 1 week from a 10 wt. % toluene solution. After drying, the sample was heated in vacuum to 60°C for 3 days to remove any residual solvent This 50-33 kg/mol PS-PDMS sample exhibits the DG structure. The second sample was a 51-35 kg/mol PS-PDMS diblock with a PDMS volume fraction of 42 % which formed a DD phase. Two sample processing methods were employed, both yielded a DD phase. A thin film sample was slowly cast over 1 week from a 10 wt.% toluene solution and after drying, the sample was heated to 60°C for 3 days with vacuum in order to remove any residual solvent. The other processing method was to fabricate BCP microspheres in which monodisperse microspheres were made from an emulsion of 6 mg/ml polymer-toluene droplets in a continuous phase of DI water containing sodium dodecyl sulfate (0.1 wt.%). With the help of nitrogen gas, the polymer solution was passed through 5.1 micron diameter pores of a Shirasu Porous Glass membrane, forming near-monodisperse microspheres stabilized by the surfactant. The concentration of toluene in the suspended microspheres decreased very slowly over 3 days due to its limited solubility in the water matrix. Subsequently, the microspheres were dispersed onto a glass slide. All samples were coated with a 50 nm protective layer of platinum for slice and view SEM.

Declaration of Competing Interest

The authors declare the following financial interests/personal relationships which may be considered as potential competing interests: Edwin L. Thomas reports financial support was provided by US Department of Energy. Edwin L. Thomas reports financial support was provided by US National Science Foundation. If there are other authors, they declare that they have no known competing financial interests or personal relationships that could have appeared to influence the work reported in this paper.

Data availability

Data will be made available on request.

CRediT authorship contribution statement

Wenpeng Shan: Conceptualization, Investigation, Writing – review & editing. **Vivek Subramanian:** Formal analysis, Investigation, Writing – review & editing. **Xueyan Feng:** Investigation, Methodology, Writing – review & editing.

Edwin L. Thomas: Conceptualization, Formal analysis, Writing – review & editing.

Acknowledgments

The authors thank G. Grason, M. Dimitriyev, B. Greenvall for stimulating discussions and valuable comments on the manuscript. We gratefully acknowledge A. Averopoulos and G. Manesi for synthesizing the PS-PDMS diblock copolymers. We also thank J. Lebeau and P. King for help with simulations of SEM slices. This research was primarily supported by the National Science Foundation, Division of Materials Research, Polymers Program, grant DMR 2105296 and by the U.S. Department of Energy (DOE), Office of Basic Energy Sciences, Division of Materials Sciences and Engineering, under award DE-SC0022229.

References

- [1] S.M. Allen, E.L. Thomas, The Structure of Materials, Wiley, 1999.
- [2] M. Kleman, Points, Lines and Walls, Wiley, New York, 1983.
- [3] A. Sutton, R. Balluffi, Interfaces in Crystalline Materials, Oxford University Press, Oxford, UK, 1995.
- [4] D.R. Nelson, Defects and Geometry in Condensed Matter Physics, Cambridge University Press, 2002.
- [5] S.P. Gido, E.L. Thomas, Lamellar Diblock copolymer grain-boundary morphology .4. Tilt boundaries, Macromolecules 27 (21) (1994) 6137–6144.
- [6] S.P. Gido, J. Gunther, E.L. Thomas, D. Hoffman, Lamellar diblock copolymer grain boundary morphology. 1. Twist boundary characterization, Macromolecules 26 (17) (1993) 4506–4520.
- [7] B.L. Carvalho, R.L. Lescanec, E.L. Thomas, in: Grain Boundary Defects in Block Copolymer Systems: Bulk and Thin Film Results, Macromol Symp, Wiley Online Library, 1995, pp. 1131–1146.
- [8] Y. Nishikawa, H. Kawada, H. Hasegawa, T. Hashimoto, Grain boundary morphology of lamellar microdomains, Acta Polym. 44 (4) (1993) 192–200.
- [9] L. Corté, K. Yamauchi, F. Court, M. Cloître, T. Hashimoto, L. Leibler, Annealing and defect trapping in lamellar phases of triblock terpolymers, Macromolecules 36 (20) (2003) 7695–7706.
- [10] X. Feng, H. Guo, E.L. Thomas, Topological defects in tubular network block copolymers, Polymer 168 (2019) 44–52.
- [11] T. Miyata, H.-F. Wang, T. Suenaga, D. Watanabe, H. Marubayashi, H. Jinnai, Dislocation-induced defect formation in a double-gyroid network, Macromolecules 55 (18) (2022) 8143–8149.
- [12] X. Feng, M.S. Dimitriyev, E.L. Thomas, Soft, malleable double diamond twin, Proc. Natl. Acad. Sci. U.S.A. 120 (4) (2023) e2213441120.
- [13] A. Jangizehi, F. Schmid, P. Besenius, K. Kremer, S. Seiffert, Defects and defect engineering in Soft Matter, Soft Matter. 16 (48) (2020) 10809–10859.
- [14] W. Li, M. Müller, Defects in the self-assembly of block copolymers and their relevance for directed self-assembly, Annu. Rev. Chem. Biomol. Eng. 6 (2015) 187–216.
- [15] Y. Kambe, C.G. Arges, D.A. Czaplewski, M. Dolejsi, S. Krishnan, M.P. Stoykovich, J.J. De Pablo, P.F. Nealey, Role of defects in ion transport in block copolymer electrolytes, Nano Lett. 19 (7) (2019) 4684–4691.
- [16] T. Segal-Peretz, J. Ren, S. Xiong, G. Khaira, A. Bowen, L.E. Ocola, R. Divan, M. Doxastakis, N.J. Ferrier, J. de Pablo, Quantitative three-dimensional characterization of block copolymer directed self-assembly on combined chemical and topographical prepatterned templates, ACS Nano 11 (2) (2017) 1307–1319.
- [17] R.A. Segalman, Patterning with block copolymer thin films, Mater. Sci. Eng.: R: Rep. 48 (6) (2005) 191–226.
- [18] S. Darling, Directing the self-assembly of block copolymers, Prog. Polym. Sci. 32 (10) (2007) 1152–1204.
- [19] I. Hamley, Ordering in thin films of block copolymers: fundamentals to potential applications, Prog. Polym. Sci. 34 (11) (2009) 1161–1210.
- [20] A. Reddy, X. Feng, E.L. Thomas, G.M. Grason, Block copolymers beneath the surface: measuring and modeling complex morphology at the subdomain scale, Macromolecules 54 (20) (2021) 9223–9257.
- [21] G.M. Grason, E.L. Thomas, How does your gyroid grow? A mesoatomic perspective on supramolecular, soft matter network crystals, Phys. Rev. Mater. 7 (4) (2023) 045603.
- [22] E.L. Thomas, D.M. Anderson, C.S. Henkee, D. Hoffman, Periodic area-minimizing surfaces in block copolymers, Nature 334 (6183) (1988) 598–601.
- [23] D. Karpov, K. Djeghdi, M. Holler, S.N. Abdollahi, K. Godlewska, C. Donnelly, T. Yuasa, H. Sai, U.B. Wiesner, B.D. Wilts, High-resolution three-dimensional

- imaging of topological textures in single-diamond networks, arXiv preprint $arXiv:2304.14819\ (2023)$.
- [24] H. Jinnai, R.J. Spontak, Transmission electron microtomography in polymer research, Polymer 50 (5) (2009) 1067–1087.
- [25] M. Kato, T. Ito, Y. Aoyama, K. Sawa, T. Kaneko, N. Kawase, H. Jinnai, Three-dimensional structural analysis of a block copolymer by scanning electron microscopy combined with a focused ion beam, J. Polym. Sci. Part B: Polym. Phys. 45 (6) (2007) 677–683.
- [26] D.A. Hajduk, P.E. Harper, S.M. Gruner, C.C. Honeker, G. Kim, E.L. Thomas, L.J. Fetters, The gyroid: a new equilibrium morphology in weakly segregated diblock copolymers, Macromolecules 27 (15) (1994) 4063–4075.
- [27] C.-Y. Chu, W.-F. Lin, J.-C. Tsai, C.-S. Lai, S.-C. Lo, H.-L. Chen, T. Hashimoto, Order-order transition between equilibrium ordered bicontinuous nanostructures of double diamond and double gyroid in stereoregular block copolymer, Macromolecules 45 (5) (2012) 2471–2477.
- [28] A.F. Wells, Three Dimensional Nets and Polyhedra, Wiley, 1977.
- [29] I. Prasad, H. Jinnai, R.-M. Ho, E.L. Thomas, G.M. Grason, Anatomy of triply-periodic network assemblies: characterizing skeletal and inter-domain surface geometry of block copolymer gyroids, Soft Matter. 14 (18) (2018) 3612–3623.
- [30] X. Feng, C.J. Burke, M. Zhuo, H. Guo, K. Yang, A. Reddy, I. Prasad, R.-M. Ho, A. Avgeropoulos, G.M. Grason, Seeing mesoatomic distortions in soft-matter crystals of a double-gyroid block copolymer, Nature 575 (7781) (2019) 175–179.
- [31] G.E. Toombes, A.C. Finnefrock, M.W. Tate, R. Ulrich, U. Wiesner, S.M. Gruner, A re-evaluation of the morphology of a bicontinuous block copolymer- ceramic material, Macromolecules 40 (25) (2007) 8974–8982.
- [32] B.J. Dair, C.C. Honeker, D.B. Alward, A. Avgeropoulos, N. Hadjichristidis, L.J. Fetters, M. Capel, E.L. Thomas, Mechanical properties and deformation behavior of the double gyroid phase in unoriented thermoplastic elastomers, Macromolecules 32 (24) (1999) 8145–8152.
- [33] J. Rabier, L. Pizzagalli, J. Demenet, Dislocations in silicon at high stress, Dislocat. Solids 16 (2010) 47–108.

- [34] A. Blumenau, R. Jones, T. Frauenheim, B. Willems, O. Lebedev, G. Van Tendeloo, D. Fisher, P. Martineau, Dislocations in diamond: dissociation into partials and their glide motion, Phys. Rev. B 68 (1) (2003) 014115.
- [35] J. Xiao, H. Yang, X. Wu, F. Younus, P. Li, B. Wen, X. Zhang, Y. Wang, Y. Tian, Dislocation behaviors in nanotwinned diamond, Sci. Adv. 4 (9) (2018) eaat8195.
- [36] X. Feng, M. Zhuo, H. Guo, E.L. Thomas, Visualizing the double-gyroid twin, Proc. Natl. Acad. Sci. 118 (12) (2021) e2018977118.
- [37] V. Gertsman, Geometrical theory of triple junctions of CSL boundaries, Acta Crystallogr. Sect. A Found. Crystallogr. 57 (4) (2001) 369–377.
- [38] S. Engström, K. Alfons, M. Rasmusson, H. Ljusberg-Wahren, Solvent-induced sponge (L 3) phases in the solvent-monoolein-water system, in: The Colloid Science of Lipids: New Paradigms for Self-Assembly in Science and Technology, Springer, 1998, pp. 93–98.
- [39] J.H. Lee, C.Y. Koh, J.P. Singer, S.J. Jeon, M. Maldovan, O. Stein, E.L. Thomas, 25th anniversary article: ordered polymer structures for the engineering of photons and phonons, Adv. Mater. 26 (4) (2014) 532–569.
- [40] L. Lu, Z. Wang, D. Ye, L. Ran, L. Fu, J.D. Joannopoulos, M. Soljac, Experimental observation of Weyl points, Science 349 (2015) 622.
- [41] M. Fruchart, S.-Y. Jeon, K. Hur, V. Cheianov, U. Wiesner, V. Vitelli, Soft self-assembly of Weyl materials for light and sound, Proc. Natl. Acad. Sci. 115 (16) (2018) E3655–E3664.
- [42] M.S. Dimitriyev, A. Reddy, G.M. Grason, Medial packing, frustration and competing network phases in strongly-segregated block copolymers, arXiv preprint arXiv:2306.02598 (2023).
- [43] H-F. Wang, H. Marubayashi, H. Jinnai, Kinetic pathway of the order-order transition from hexagonally packed cylinder to hexagonally perforated layer in polystyrene block-Poly(2-vinylpyridine) using time-resolved 3D transmission electron microtomography, Macromolecules 56 (2023) 1503–1513.
- [44] C. Chang, G-M. Manesi, C-Y. Yang, Y-C. Hung, K-C. Yang, P-T. Chiu, P-T.A. Avgeropoulos, R.M. Ho, Mesoscale networks and corresponding transitions from self-assembly of block copolymers, in: Proceedings of the National Academy of Sciences, 118, 2021 e2022275118.